Article

Analysis of nonlinear intensity attenuation in bright-field TEM images for correct 3D reconstruction of the density in micron-sized materials

Jun Yamasaki[1,2,*], Michihiro Mutoh[3], Shigemasa Ohta[4], Syuichi Yuasa[4], Shigeo Arai[2], Katsuhiro Sasaki[5], and Nobuo Tanaka[2]

[1]Research Center for Ultra-High Voltage Electron Microscopy, Osaka University, 7-1 Mihogaoka, Ibaraki, Osaka 567-0047, Japan, [2]EcoTopia Science Institute, Nagoya University, Furo-cho, Chikusa-ku, Nagoya 464-8603, Japan, [3]Department of Crystalline Materials Science, Nagoya University, Furo-cho, Chikusa-ku, Nagoya 464-8603, Japan, [4]JEOL Ltd., 3-1-2 Musashino, Akishima, Tokyo 196-8558, Japan, and [5]Department of Quantum Engineering, Nagoya University, Furo-cho, Chikusa-ku, Nagoya 464-8603, Japan

*To whom correspondence should be addressed. E-mail: yamasaki@uhvem.osaka-u.ac.jp

Abstract

To obtain the correct tomographic reconstruction of micron-sized materials, the nonlinear intensity attenuation of bright-field transmission electron microscopy (BF-TEM) images was analyzed as a function of the sample thickness using a high-voltage electron microscope. The intensity attenuation was precisely measured relative to the projection thickness of carbon microcoils (CMCs) at acceleration voltages of 400–1000 kV using objective apertures (OAs) with radii of 2.1–28 nm^{-1}. The results show that the nonlinearity is strongly dependent on the OA size and the acceleration voltage. The influence of nonlinearity on tomographic reconstructions was also examined using a specially developed 360°-tilt sample holder. Sliced images of the reconstructed volumes indicated that an increase in the nonlinearity caused artificial fluctuations in the internal density of materials and inaccurate shapes of the objects in more significant cases. Conditions sufficient for reconstruction with the correct density have been estimated to be 0.67 of the minimum electron transmittance, and for reconstructions with correct shapes, 0.4. This information enables foreseeing the quality of the reconstruction from a single BF-TEM image prior to the tilt-series acquisition. As a result to demonstrate the appropriateness of these conditions, a CMC with a diameter of 3.7 µm was reconstructed successfully; i.e. not only the shape but also the internal density were correctly reproduced using electron tomography.

Key words: electron tomography, bright-field TEM, nonlinear intensity attenuation, HVEM, 360°-tilt sample holder, carbon microcoil

Introduction

Currently, 3D analyses of nanometer- and sub-micron-sized objects are extensively performed by tomography using transmission electron microscopes (TEM) in various imaging modes suitable for each purpose. For example, since the first report in 2001 [1], electron tomography based on annular dark-field scanning TEM (ADF-STEM) has been successfully applied to observing the 3D structures of crystalline materials [2–4], owing to the image contrast insensitive to the diffraction conditions. Active utilization of the diffraction contrast in bright-field STEM and dark-field TEM has enabled the 3D analysis of embedded structures in bulk crystalline materials such as dislocations and precipitates [5–7]. On the other hand, various non-crystalline objects such as biological samples [8–10], polymers [11] and other inorganic materials [12,13] have been widely analyzed by bright-field TEM (BF-TEM) tomography. Among the various imaging modes in TEMs, BF-TEM is the most basic and simplest mode. BF-TEM tomography has an advantage that the images used for the reconstruction are free from local distortions due to sample drift unlike STEM. Another practical advantage is that adhesion of contaminants on samples via parallel illumination, which is sometimes a problem for scanning focused probes, is not a serious issue in BF-TEM.

In electron tomography using medium-voltage TEMs, the size and thickness of samples are limited to be <1 μm [1–5,11–19]. To extend the observable range to the micron scale, increasing the acceleration voltage is essential. Several achievements in 3D observations of micron-sized materials have been reported using BF-TEM tomography in a high-voltage electron microscope (HVEM) [8–10,20]. The 3D surface morphology of such micron-sized materials can be, however, observed also using scanning electron microscopy (SEM). Therefore, the important capability required in transmission electron tomography is not only the qualitative determination of 3D shapes but also the quantitative analysis of the 3D data, particularly the data for the interior of micron-sized objects.

One of the important issues on the quantitative 3D analyses is the missing-wedge effect, which is induced by the limited tilt angles because of the sample holder design and/or the sample configuration itself. The most reliable and straightforward solution is to acquire a tilt series over the entire angular range. This approach has been achieved to date by some researchers using pillar samples attached to special sample holders [16,21,22]. Because the reconstructed volumes in the results are free from the elongation artifacts, quantitative information on the 3D shapes, such as superficial areas and volume fractions of embedded grains in bulk, has been obtained [16]. Unlike such quantitative '3D shape reconstruction', procedures for achieving the

correct 3D reconstruction of internal density have not yet been established. Such '3D density reconstruction' is required for the discrimination of materials and voids [15,20] and for the detection of gradual compositional changes in various materials [19], which are often induced by intermixing in multilayer films and core-shell particles.

In addition to eliminating the missing-wedge effects, increasing the accuracy of the projection information for 3D objects is also indispensable to the 3D density reconstructions. According to the principle of tomographic reconstruction, the signals in a projection image must be proportional to the projection mass–thickness (density integrated along the beam direction). Therefore, prior to the reconstruction procedure, the image intensity of the micrographs in a tilt series must be converted to the 'proportional' signals. However, this conversion is only possible when the image intensity and sample thickness are correlated by a known monotonic relationship. BF-TEM image intensity basically changes when a portion of the scattered electrons are stopped by the objective aperture (OA) and/or other fixed apertures in the column of the microscope (scattering contrast) [23]. When the diffraction contrast is negligibly small, the scattering contrast becomes the mass–thickness contrast, which reflects the composition and atom density of the material as well as the thickness. Under a kinematical approximation, the BF-TEM image intensity based on the mass–thickness contrast exhibits exponential attenuation with increasing thickness. The beam intensity $I(t)$ over a sample area with a thickness t is shown as follows:

$$I(t) = I_0 \exp(-\mu t), \tag{1}$$

where I_0 is the incident beam intensity and μ is the attenuation coefficient, which is dependent on the scattering cross section of the material and the OA size. Therefore, the electron transmittance $T(t)$ given by $I(t)/I_0$ exhibits linear attenuation on a semi-logarithmic scale:

$$\ln T(t) = -\mu t. \tag{2}$$

However, the BF-TEM image intensity in actual experiments deviates from this linear attenuation due to multiple elastic/inelastic scatterings with increasing sample thickness [23–26]. Importantly, if the linearity has collapsed in images used for a tilt series, the inaccurate mass–thickness information will be transformed into an inaccurate density distribution during the 3D reconstruction [14,15,17–19,27–29].

Currently, a large percentage of electron tomography results may be disturbed more or less by several factors such as the missing-wedge effect, the nonlinear attenuation effect and the diffraction contrast for crystalline samples. In the present study, to focus on analyzing the nonlinear

attenuation effect in BF-TEM images, a special experimental setup was prepared. The samples were amorphous carbon microcoils (CMCs) [30–35] with well-defined shapes and compositional homogeneity, which is beneficial for thickness estimation. Measurements of the nonlinearity over a wide range of acceleration voltages were conducted using an HVEM. Moreover, a 360°-tilt tomography sample holder designed specifically for the HVEM was utilized to eliminate the missing-wedge effect.

Experimental

HVEM and newly developed sample holder for 360°-tilt tomography

The HVEM at Nagoya University (JEOL: JEM-1000KRS) [10] was used for analyzing the intensity attenuation with increasing sample thickness and for acquiring the tomographic tilt series. BF-TEM images of CMCs were taken using a $2K \times 2K$ CCD camera (Gatan: ORIUS™) at acceleration voltages of 400, 600, 800 and 1000 kV. For comparison, zero-loss images with an energy window of 10 eV were also recorded using a postcolumn imaging filter (Gatan: GIF Quantum™). For 3D reconstruction of a several micrometer-sized object, the images in the tilt series must have fields of view larger than the object, e.g. ~10 μm. In the HVEM, the lowest magnification possible while keeping the objective lens power on (namely, not in LowMag mode, but in Mag mode for JEOL microscopes) is 400, which enables the recording of a 25×25 μm^2 region using the CCD camera. In the current study, a magnification of 1000, which is suitable for observing a CMC with a diameter of 3.7 μm, was selected.

The OA size is a deciding factor for the BF-TEM image contrast and therefore also for the intensity attenuation. The HVEM has four OA sizes, which are denoted as OA1, OA2, OA3 and OA4 in descending order of the radii. In Fig. 1a, their collection semi-angles $\alpha = 24.3$, 13.2, 6.80 and 1.86 mrad are compared with the halo-ring pattern taken at 1000 kV from a CMC. Although the halo rings are formed by the diffracted beams from the amorphous structure, in this paper the term 'BF-TEM' also refers to images taken with OA1–OA3. The HVEM was designed in such a way that scaling at the back-focal plane of the objective lens did not change much when the acceleration voltage was changed. In fact, the spatial frequency $\sin \alpha / \lambda$ (λ: wavelength) for the collection angles at 400 kV were measured to be nearly the same as those at 1000 kV (only ~10% larger than at 1000 kV). In this paper, the notation for the imaging conditions is in the format 1000 kV–OA3, which indicates the use of 1000 kV and OA3.

Figure 1b shows the tip section of the sample holder specially developed for the HVEM. The holder has an internal
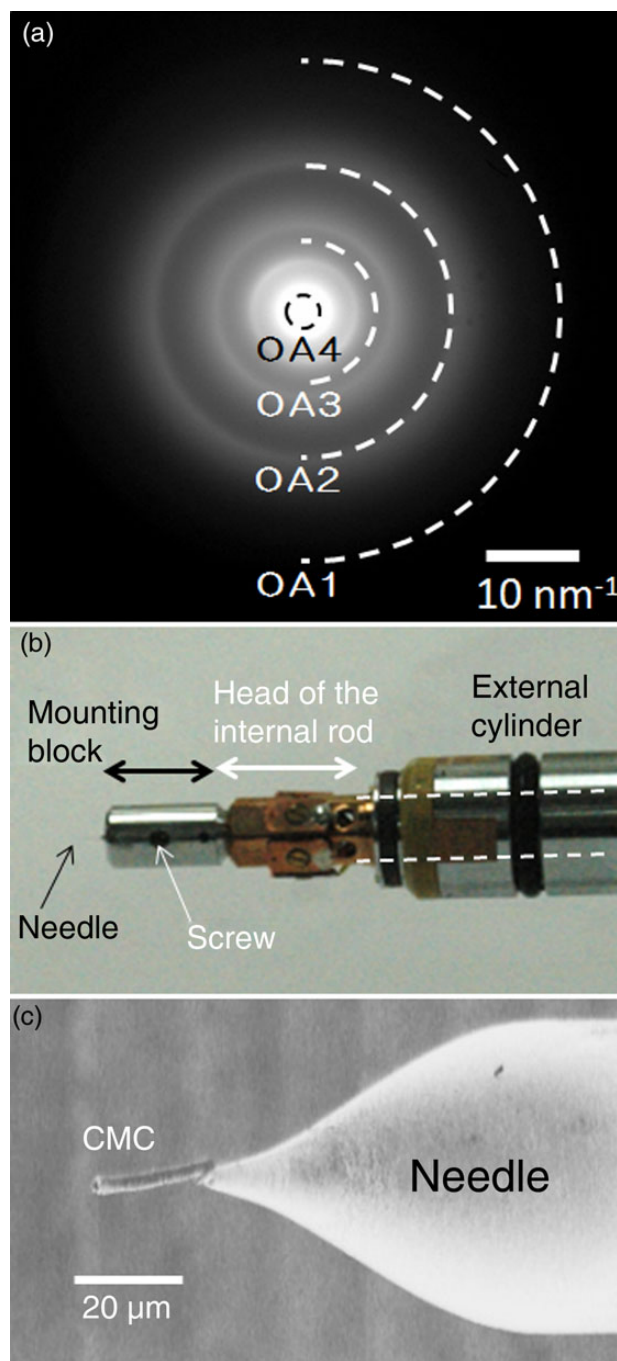

Fig. 1. (a) Sizes of the OAs compared with a halo-ring pattern from a CMC taken at 1000 kV. The collection semi-angles $\alpha = 24.3$, 13.2, 6.80 and 1.86 mrad (27.9, 15.2, 7.82 and 2.13 nm^{-1}, respectively) were calibrated based on the diffraction pattern of a silicon crystal. (b) Newly developed sample holder for HVEM tomography. The shape of the internal rod is indicated by the white broken lines. The rod is rotatable over 360° with respect to the external cylinder. (c) Scanning ion microscopy (SIM) image of a CMC fixed at the needle attached to the head of the internal rod.

rod that is rotatable over 360° with respect to the external cylinder. For tomographic observations, a sample is initially attached to the tip of a tungsten needle in a focused ion beam instrument (in the present study, Hitachi: FB-2100

was used) (Fig. 1c). Then the needle is inserted into the central hole of the mounting block and fixed by a screw (see Fig. 1b). Finally, the mounting block is screwed into the head of the internal rod. For each tilt series described below, 176 images were recorded from 0.0° to 179.4° with exposure times of 1–2 s. The last image of each series nearly coincides with the reverted first image, which confirms that no significant deformation of the sample occurred due to radiation damage or sputtering effects during the tilt-series acquisitions. The tilt-series images were processed for 3D reconstruction using commercially available software (TEMography™, System In Frontier Inc.). As fiducial markers for image alignment, small particles on the CMC, such as tungsten clusters adhered during the fixing process to the needle (shown later in Fig. 3a), were used. The reconstructions were performed using the standard filtered back-projection method.

Carbon microcoils

To exclude the missing-wedge effect and to determine the relationship between the sample thickness and image intensity, the sample must have a well-defined, rod-like shape. In addition, to focus on multiple scattering effects, uniform amorphous materials are desirable due to the minimized diffraction contrast in their BF-TEM images. Thus, to meet all of the above requirements, CMCs are considered to be one of the best choices. Figure 2a and b shows micrographs of the CMCs (Microphase Co., Ltd.) used in the present study. These helical, amorphous carbon fibers, most of which are double helical, are grown via the pyrolysis of acetylene using catalytic metal particles such as nickel [30]. Because of their characteristic helical morphology, a typical diameter on the micron scale and conductive properties [33], CMCs are expected to have applications such as radio wave absorbents, tactile sensors [32,34].

Although the 3D structure of CMCs has been roughly examined using scanning confocal electron microscopy [35], precise 3D observations via electron tomography have not yet been achieved, probably due to the inability of the electrons in medium-voltage TEMs to penetrate micron-sized thick samples. Figure 2b shows a BF-TEM image of the CMC attached to the 360°-tilt sample holder in the HVEM. If the cross section of the carbon fiber has a circular shape, the surface of one fiber of the double helix is drawn using a series of points (x, y, z) that satisfy the following equations:

$$
\begin{aligned}
x &= (R + r \cos \varphi) \cos \theta \\
y &= (R + r \cos \varphi) \sin \theta \\
z &= p \frac{\theta}{2\pi} + r \sin \varphi \\
&(0 \leq \theta < 2\pi, \quad 0 \leq \varphi < 2\pi),
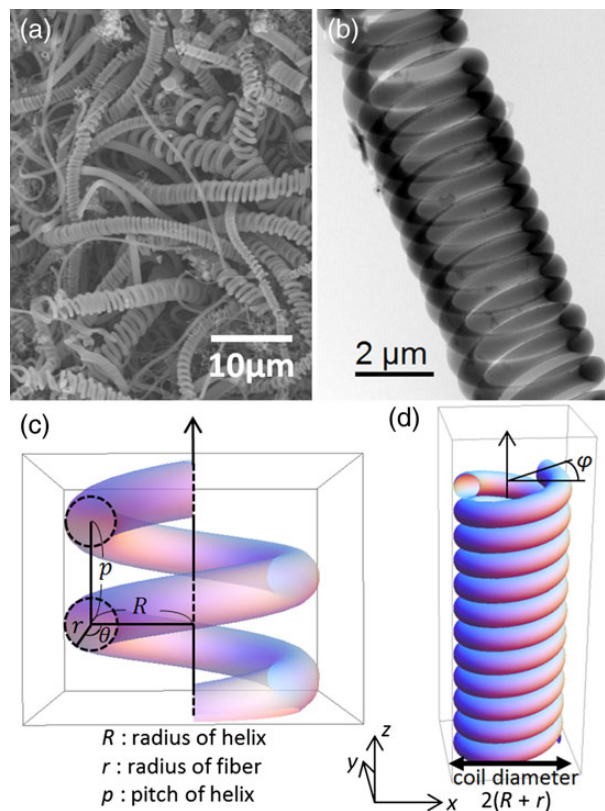\end{aligned}
\tag{3}
$$

Fig. 2. Carbon microcoils. (a) SEM image (taken by Microphase Co., Ltd.) and (b) BF-TEM image using the HVEM. (c) Parameters for the helical structure and (d) a view of the constructed model.

where R and ϕ are the radius and azimuth angle of the helical structure, and r and θ are the radius and azimuth angle of the circular cross section of the fiber (see Fig. 2c). The parameter p is the pitch of the helix, which should be $4r$ for an ideally tight double helix. The second fiber of the helical pair is reproduced in the same manner using a translation of $p/2$ in the z direction. Figure 2d shows an example of the model constructed using Eq. (3).

Results

Comparison of the experimental images and results for the structural model

Figure 3a shows a BF-TEM image of a CMC with a diameter of 3.7 μm taken at 1000 kV–OA1. Numerous particles attached to the surface (indicated by the arrows) were used later as the fiducial markers in the 3D reconstruction. The projection thickness for the model in Fig. 2d is shown in Fig. 3b and is bilaterally symmetric, unlike the image in Fig. 3a. This difference is observed because the coil axis in (a) is not perpendicular to the beam direction. When the coil axis of the model was tilted ~5°, the projection (Fig. 3c) was in good agreement with the image presented in Fig. 3a. As seen in Fig. 2a and b as well as in the lower half of Fig. 3a, local fluctuations of the
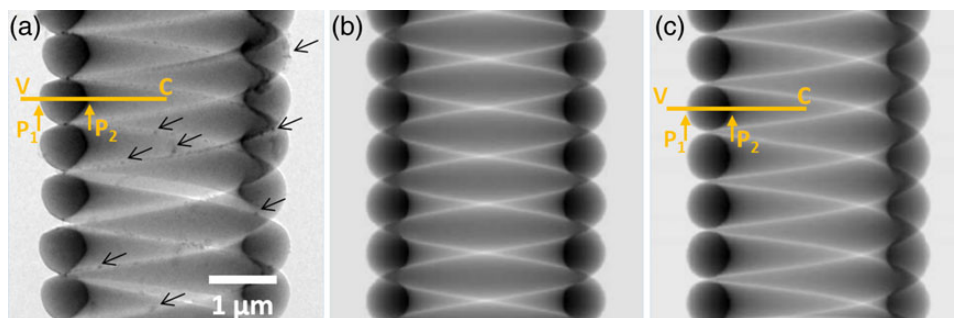
Fig. 3. CMC with a diameter of 3.7 μm. (a) BF-TEM image taken at 1000 kV–OA1. Projections of the model structure (b) without tilt and (c) tilted 5°. The black arrows in (a) indicate the clusters used as the fiducial markers.

helical pitch and loosening of the interlocked helical pair occurred. For precise comparisons free from such uncertainties, the image intensity was analyzed along the line in Fig. 3a, in which the helical pair was tightly interlocked. The line runs from a position V in the vacuum to the coil center C and passes through the thickest part of the sample near P_2.

The intensity profile measured in Fig. 3a was normalized using the vacuum intensity I_0 to show the electron transmittance T. As can be seen in Fig. 4a, when the attenuation coefficient μ is 1.0×10^{-4} nm^{-1}, the profile of $-\ln T/\mu$ agrees well with the thickness profile in Fig. 3c. Although the agreement is best for a tilt angle of 5°, the thickness profiles between P_1 and P_2 are insensitive to the slight estimation error of the tilt angle. There are, however, discrepancies between the measured profile and the model in the areas near P_1 and P_2. In Fig. 4a, the positions where the discrepancies start are represented as P_1' and P_2', which correspond to the thickness of 1200 and 2700 nm, respectively. As mentioned also in the section Nonlinear intensity attenuation dependence on the OA size and acceleration voltage, it is generally known that the nonlinear attenuation makes BF-TEM image brighter than expected from the linear attenuation [23–26]. Against the general tendency, the image intensity in the areas $P_1 - P_1'$ and $P_2' - P_2$ is darker than expected from the model and thus cannot be explained by the nonlinearity. As shown schematically in Fig. 4b, P_1 and P_2 correspond to the object edges for the transmitted electrons. In Fig. 3a, the fiber cross section appears to have a polygonal shape rather than a circular shape, which possibly originates from the polyhedral shape of the catalytic cluster [31]. The projection thicknesses near the edges are considered to be sensitive to the cross-sectional shape and tend to deviate from the calculation based on the circular shape. Thus, it is considered that the darker image contrasts in $P_1 - P_1'$ and $P_2' - P_2$ do not originate from the nonlinearity, but indicate the actual thicknesses.

The electron transmittance was also measured under the energy-filtered condition. Figure 4c presents a zero-loss image

for the area near the line in Fig. 3a taken at 1000 kV–OA1. The profile of $-\ln T/\mu$ measured along $V' - C'$ in Fig. 4c is shown in Fig. 4a. The value of μ has been optimized to be 2.7×10^{-3} nm^{-1} such that the energy-filtered profile is in agreement with the unfiltered profile for the thinner area of the sample. However, for the areas thicker than 1 μm, the profile is saturated and never corresponds to the thickness. Therefore, with respect to the linearity, unfiltered BF-TEM images are preferable to filtered ones, because the linearity of the latter is largely limited to areas with a thickness of 1 μm even when observed at 1000 kV.

Nonlinear intensity attenuation dependence on the OA size and acceleration voltage

Using the data between P_1 and P_2 in Fig. 4a, the relationship between $\ln T$ and the sample thickness was plotted in Fig. 5a (indicated by OA1). Because the thickness estimation in the areas $P_1 - P_1'$ and $P_2' - P_2$ is difficult as mentioned previously, only the thickness range between 1200 and 2700 nm is available for analysis of the relationship between thickness and transmittance (hereafter, referred to as 'specified thickness range'). Figure 5a shows also the least squares fitted line for the subset in the specified thickness range, which has a slope $\mu = 1.0 \times 10^{-4}$ nm^{-1} and passes exactly through the origin. This result indicates that the intensity attenuation at 1000 kV–OA1 has a good linearity up to ∼3 μm or more.

Figure 5a also shows the intensity attenuation obtained with OA2, OA3 and OA4 at the same position and in the same manner as with OA1. Because a BF-TEM image is formed by electrons passing through the OA, the intensities obtained with smaller OAs are smaller than that with the larger OA over the entire thickness range. It can be seen in Fig. 5a that the data with smaller OAs fall in curved rather than straight lines. This behavior can be visualized more clearly by considering the intercepts of the least squares fitted lines at zero thickness. For example, at a glance, the data with OA2 in the specified thickness range fall in a
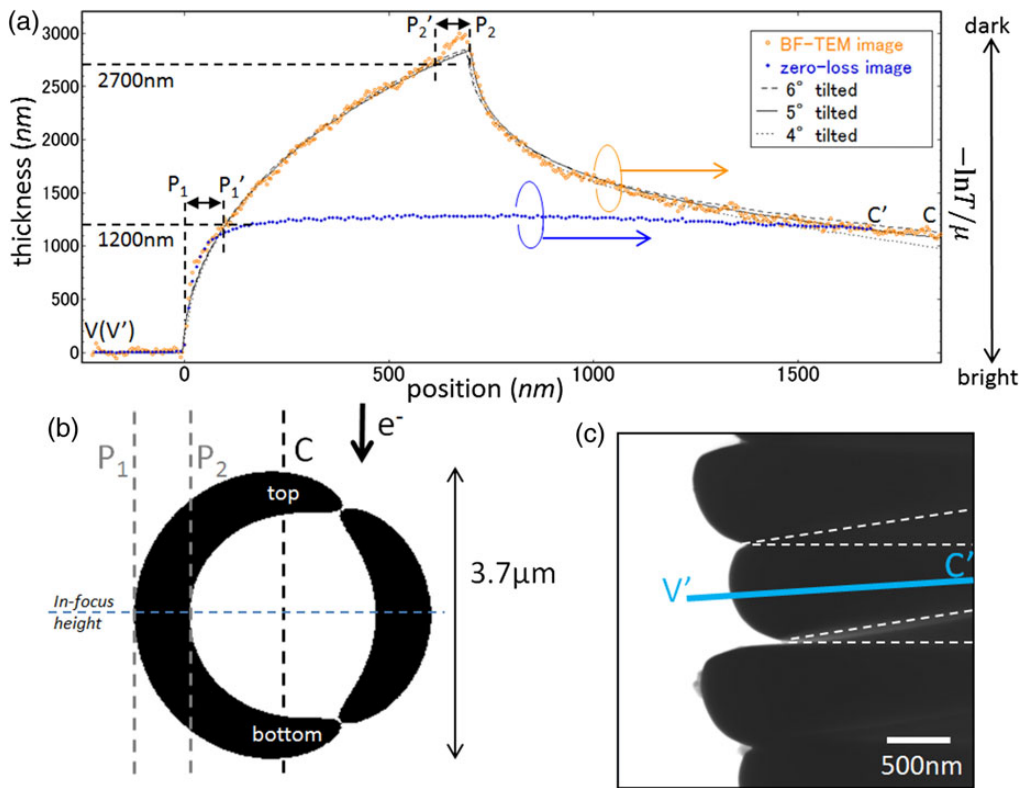
Fig. 4. Comparison of the projection thickness of the structural model and electron transmittance. (a) Profiles along the lines in Figs 3a, c and 4c. The model projections were calculated for coil axis tilts of 4°, 5° and 6°. The μ values are 1.0×10^{-4} and 2.7×10^{-3} nm^{-1} for the BF-TEM and zero-loss images, respectively. (b) Schematic of the cross section of the CMC along the electron transmission. (c) Zero-loss image of the CMC. The shape of the fiber is indicated by the broken lines.
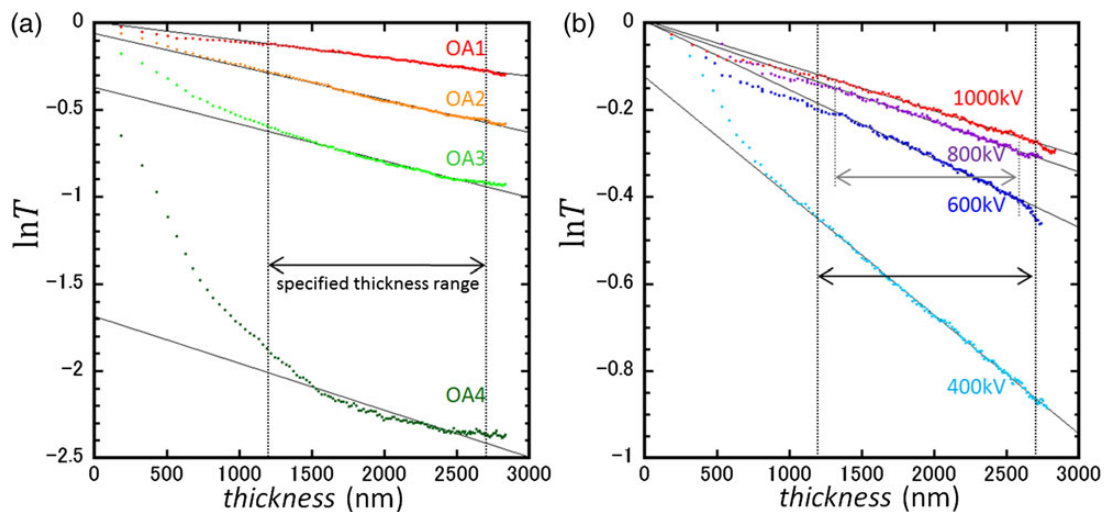

Fig. 5. Intensity attenuation in BF-TEM images with increasing thickness. (a) Dependence on the OA size at 1000 kV. (b) Dependence on the acceleration voltage with OA1. Least squares fitted lines for the data in the specified thickness ranges (1200–2700 nm for 400 and 1000 kV and 1300–2600 nm for 600 and 800 kV) are also shown.

straight line. However, the negative value of the intercept indicates that the intensity attenuation does not exactly undergo exponential decay.

Figure 5b shows the attenuation at acceleration voltages of 400, 600, 800 and 1000 kV with OA1. The smaller intensities at the lower voltages reflect the differences in

penetration capability. Because the data at 600 and 800 kV were obtained using another CMC, the specified thickness range is slightly different from that for the results at 400 and 1000 kV. In these ranges, the data at any voltages seem to exhibit linear attenuation. However, similar to the results at 1000 kV–OA2, OA3 and OA4 in Fig. 5a, the data at 400 kV–OA1 show a considerably negative intercept value at zero thickness. Such a pseudo-linear attenuation feature has been observed also in previous reports [17,24,25], although the cause is as yet unclear. However, such nonlinear attenuation certainly introduces error in the conversion from intensity to thickness, and thus inhibits correct 3D reconstruction. In summary, smaller OAs and lower acceleration voltages increase the degree of the nonlinearity of the intensity attenuation.

3D reconstruction of a CMC sample

Tomographic tilt series were acquired for the CMC in Fig. 3a at the three characteristic conditions shown in Fig. 5, i.e. 1000 kV–OA1, 400 kV–OA1 and 1000 kV–OA4. Sequential views of the tilt series indicated that the CMC axis was inclined ~25° from the rotation axis, which was foreseen in Fig. 1c. The results for the 3D reconstructions are shown in Fig. 6. Regardless of the differences in the imaging conditions, the 3D shape of the CMC (and also the dust attached to it) has been reconstructed well. This means that the substantial degrees of the nonlinearity observed in Fig. 5 do not hinder overviews of 3D objects.

For detailed comparisons, the cross sections of the 3D volumes were then examined. Figure 7a shows a sliced image of the structural model when cutoff as shown in the lower portion of the figure. The normal direction of the slice is parallel to the rotation axis and thus inclined 25° from the coil axis. Figure 7b–d shows corresponding images sliced from the reconstructed volumes in Fig. 6a–c, respectively. The profile in Fig. 7b confirms that the material and vacuum have been reconstructed with the respective uniform

intensity (apart from the enhanced edges, which are discussed later). In contrast, the internal density of the CMC in Fig. 7c is not uniform, but has a gradient from the center. Moreover, there is a slight increase in the vacuum level in the interior of the coil. These features are more significant in Fig. 7d, in which also the shape of the CMC has been incorrectly reproduced. In particular, the interior region is so blurred that the inner walls are difficult to identify. In Fig. 7c and d, the artificial streaks are remarkable in the vacuum regions. However, the direct effect of the nonlinearity has not yet been clarified. As can be seen in Fig. 5, not only the linearity but also the total intensity decrease in the order Fig. 7b > c > d. Such dark images tend to decrease the precision of the alignment using fiducial markers. Apart from such a practical problem, these results do demonstrate that 3D density reconstructions of a 3.7 μm-sized material are achievable using 1000 keV electron beams.

Discussion

Nonlinear attenuation caused by multiple scatterings

In a material, a portion of the incident electrons is scattered to the angular region larger than the OA radius. During passage through the material, these electrons can be scattered again back to the angular region inside the OA with a certain probability. Consequently, at the exit surface of the sample, the number of electrons inside the OA becomes greater than expected based on kinematical single scatterings. Thus, these multiple scatterings make the attenuation of the BF-TEM intensity more gradual than the ideal linear attenuation, as seen in the curves with OA3 and OA4 in Fig. 5a. Based on the above consideration, the deciding factor should be the angular distribution of the scattered electrons. Roughly speaking, a greater number of electrons outside of the OA lead to more the scattered-back electrons.
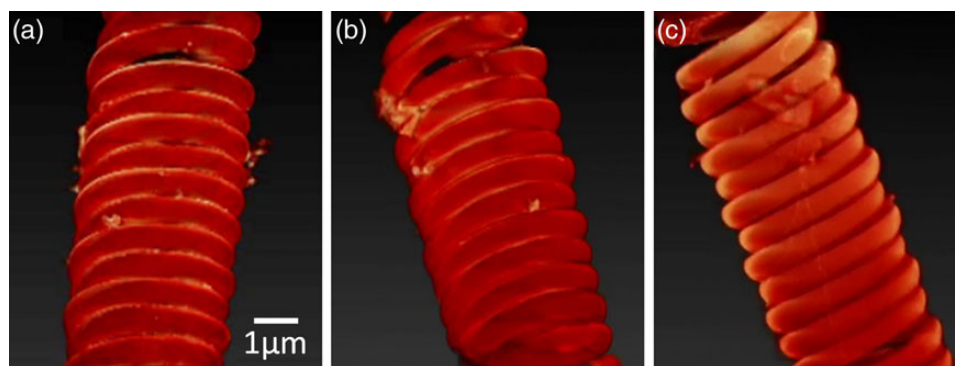

Fig. 6. Volume-rendered views of the reconstructed volumes for the same CMC observed at (a) 1000 kV–OA1, (b) 400 kV–OA1 and (c) 1000 kV–OA4.
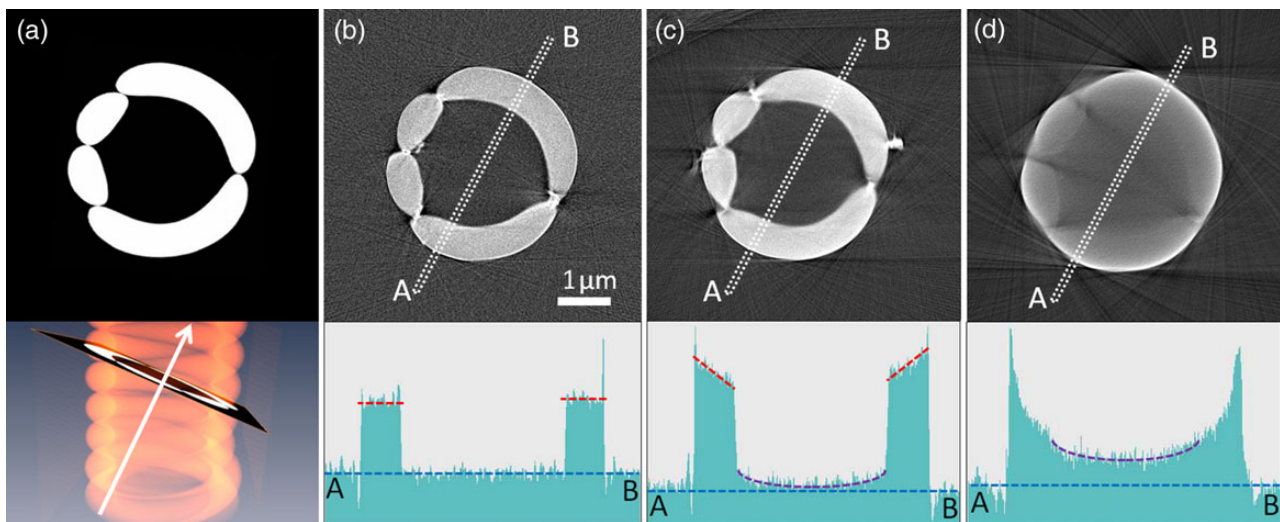
Fig. 7. Comparison of sliced images. (a) Structural model and reconstructed volumes at (b) 1000 kV–OA1, (c) 400 kV–OA1 and (d) 1000 kV–OA4. The bright and dark regions correspond to the material and vacuum, respectively. The normal direction of the slice is parallel to the rotation axis as shown in the lower part of (a). Line profiles between A and B are also shown in (b–d).

This tendency can be seen in Fig. 5a, in which the nonlinear characteristics increase when a smaller OA is used. However, this result conflicts with a previous report using 2 MeV electron beams, in which no change of the linearity due to the OA size was observed [24]. In that report, the linearity was estimated from only several measurement data sparsely sampled in a thickness range near zero thickness. In such a thinner range, because the nonlinear curves deviate only slightly from a straight line, precise estimation of the nonlinearity could be difficult. However, in the present study, the nonlinearity has been estimated from a lot of measurement data densely sampled in the thicker ranges (Fig. 5), where the nonlinear attenuation becomes much more significant. Thus, the contradiction between the previous and the present reports may be due to the level of precision of the measurements. Regarding Fig. 5b, the data at 1000 kV show much larger transmittance and better linearity than that at 400 kV. This result is expected, because smaller scattering cross sections for higher energy electrons result in smaller numbers of electrons scattered to the outside of the OA. Thus, both the OA and acceleration voltage must be selected carefully to control the nonlinearity and quality of 3D reconstructions.

The above discussion of multiple scatterings should be valid without distinction between elastic and inelastic processes. Based on the elastic and inelastic scattering cross sections of atoms, the linear attenuation coefficient μ_{BF} for BF-TEM image intensity is calculated to be [23]

$$\mu_{BF} = \frac{\rho N_A Z^{1/3} \lambda^2}{\pi A} \left(1 + \frac{E}{E_0}\right)^2 \left\{\frac{b-1}{b}(Z-1) + 2 \ln b\right\},$$

$$b = 1 + \left(\frac{Z^{1/3}\lambda}{2\pi\alpha a_H}\right)^2 \tag{4}$$

for a material which has a density ρ and consists of a light element with atomic number Z and atomic weight A (6 and 12 for CMCs, respectively). N_A is Avogadro constant, a_H Bohr radius, E_0 and E rest energy and kinetic energy of the incident electrons, respectively. Assigning the measured value 1.0×10^{-4} nm^{-1} to μ_{BF}, ρ is estimated to be 1.9 g/cm^3. As shown in Fig. 4c, a large fraction of electrons is lost in the zero-loss image if the sample is thicker than 1 μm. This means that the corresponding unfiltered BF-TEM intensity is mostly formed by inelastically scattered electrons. Note that the contribution of plasmon scattering is not considered in Eq. (4). Nevertheless, the estimated ρ agrees with the density generally known for amorphous carbons (1.8–2.1 g/cm^3). This good agreement indicates that, in the thickness range of the linear attenuation, deflection angles by plasmon scatterings are much smaller than the OA radius (24.3 mrad) and therefore do not contribute to the intensity attenuation in the unfiltered BF-TEM image so much. On the other hand, if the thickness increases up to the nonlinear attenuation range, the angular spread by multiple plasmon scatterings could become too large to be negligible compared with the OA radius. This behavior may be the reason why experimental nonlinear attenuations are not reproduced with a high degree of accuracy by the mathematical model based on a statistic treatment of multiple elastic scatterings [24,25]. Clarification of the angular distribution of the multiple inelastic scatterings is required to elucidate the functional form of the nonlinear attenuation more accurately. Further studies will lead to corrections for the nonlinear curvatures, as has been achieved for incoherent BF-STEM and HAADF-STEM tomography [15,19].

Influence of nonlinear attenuation on 3D reconstructions

In Fig. 5, the values of ln T at the maximum thickness t_{max} are approximately −0.9 at 400 kV–OA1 and −2.4 at 1000 kV–OA4. The corresponding transmittance $T(t_{max})$ at the maximum thickness is 0.4 and 0.09, respectively. The threshold value for accurate 3D shape reconstructions should exist somewhere between them. It is interesting that this range is nearly coincident with the threshold transmittance of 0.1 using energy-filtered images [14,17], despite the difference of the contrast generation mechanism. The peculiar coincidence may imply a type of universality for BF-TEM image contrasts regardless of energy filtering.

The common feature in Fig. 7c and d is the gradient of the internal density from the center. This phenomenon is known as the 'cupping effect' in the field of X-ray tomography, and results from the nonlinearity induced by different absorption coefficients for each X-ray energy [27–29]. In electron tomography, dips in the density and edge enhancements have been reported to appear in the reconstructed volumes of convex dense objects, such as particles and rods, when ADF-STEM images in the tilt series include the nonlinearity or saturated intensity [18,19]. Our sample has a more complicated 3D configuration, i.e. a tubular structure with inner concave surfaces. Figure 7c and d shows that edge enhancement does not occur for such inner concave surfaces. Nevertheless, the reconstructed density in the internal space is artificially higher, as if some low-density materials are present. This result indicates that one should be careful, particularly when observing 3D structures with cavities or those that contain low-density materials in the interior, such as tubular, mesoporous and core-shell structures.

Judging from the intercept values in Fig. 5b, the data obtained at 600, 800 and 1000 kV exhibit the linear attenuation, and thus they should bring the correct 3D density reconstructions as shown in Fig. 7b. In Fig. 5b, ln $T(t_{max})$ is approximately −0.4 at 600 kV–OA1, which corresponds to $T(t_{max}) = 0.67$. Assuming the minimum transmittance as a good criterion for correct 3D density reconstruction, the threshold $T(t_{max})$ should exist between 0.4 and 0.67. In other words, whenever two-thirds of the incident electrons remain inside the OA, the 3D density reconstructions are achievable. This information should be beneficial for practical tomography experiments, because the attainability of the 3D density reconstructions can be foreseen from a single BF-TEM image prior to tilt-series acquisition.

Based on the above criterion, the attenuation coefficients measured in Fig. 4a are discussed again. The number of electrons contributing to a zero-loss image is reduced by both of

the energy window and the OA. Instead of Eq. (1), the attenuation of zero-loss intensity I_{zl} is therefore shown as

$$\begin{aligned} I_{zl}(t) &= I_0 \exp(-\mu_{BF}t)\exp(-\mu_{inel}t) \\ &= I_0 \exp[-(\mu_{BF} + \mu_{inel})t], \end{aligned} \quad (5)$$

where μ_{inel} is the attenuation coefficient due to the energy filtering. Using $\mu_{BF} = 1.0 \times 10^{-4}$ nm^{-1} and $\mu_{BF} + \mu_{inel} = 2.7 \times 10^{-3}$ nm^{-1} measured in Fig. 4a, the total-inelastic mean free path is estimated to $\lambda_{inel} = 1/\mu_{inel} = (2.7 \times 10^{-3} - 1.0 \times 10^{-4})^{-1} \simeq 380$ nm. As shown in Fig. 4a, the maximum thickness for the linearity in the zero-loss image is 1 μm, which is ~260% of $1/\mu_{inel}$. On the other hand, according to the linearity criterion as $\mu_{BF} \times t_{max} = -\ln T(t_{max}) = 0.4$–0.67, the maximum thickness t_{max} for the linearity in unfiltered BF-TEM images is only 40–67% of $1/\mu_{BF}$. The difference should be collateral evidence that the nonlinear intensity attenuation in unfiltered BF-TEM images is induced by the scattered-back electrons from outside of the OA; in contrast, energy-loss electrons have no chance to come back into the zero-loss window to form a filtered image.

Influence of Fresnel fringes on 3D reconstructions

The remaining problem in the reconstructions at 1000 kV–OA1 is the unnaturally bright rim of the fiber cross section in Fig. 7b. It has been reported that edge-enhanced images in tilt-series cause edge-enhanced 3D reconstructions [18]. In our case, it is suspected that Fresnel fringes in the BF-TEM images have induced the edge enhancement in the reconstructed volumes. As for the image in Fig. 3a, all images in the tilt series were taken at the in-focus condition for the outer edges (P_1 in Fig. 3a) of the CMCs. Therefore, the top and bottom positions shown in Fig. 4b were at the out-of-focus conditions of ~1.8 μm. The Fresnel fringe contrast around the fiber edges in the top and bottom positions should be superimposed on the mass–thickness contrast, although it is difficult to see in Fig. 3a due to the overlap of the fibers.

Because the Fresnel fringe contrast does not correspond to the projection thickness of an object, it must cause errors in the quantitative 3D reconstructions, particularly for samples with intricate surface morphologies such as mesoporous materials. Fresnel fringes are explained based on wave optics as a blurring effect of the edges induced by lens defocusing. In geometric optics, a corresponding simplified discussion of the blurring d_b is presented in terms of the depth of field $D_F = d_b/\alpha$ [36]. According to the formula, decreasing the OA radius α is effective for increasing the depth of field toward 1.8 μm. In other words, the Fresnel fringe contrast for the out of focus of 1.8 μm can be reduced by using a smaller OA. However, this solution enhances the nonlinear attenuation,

as clarified in the present study. The trade-off relationship thus limits the maximum thickness for more complete density reconstructions without edge enhancement. Clarification of the optimal conditions and the maximum mass thickness should therefore be the next target of research.

Conclusions

The nonlinear attenuation of the mass–thickness contrast in BF-TEM images with increasing thickness and its influence on 3D reconstructions were analyzed. It was clarified that the nonlinearity was sensitively affected by the OA radius and the acceleration voltage. In fact, using the largest OA and 1000 kV electron beams, a CMC with a diameter of 3.7 μm was reconstructed so successfully that not only the shape but also the internal density was correctly reproduced. We also succeeded in rough estimations of the conditions that the minimum electron transmittance of 0.4 and 0.67 are sufficient for the 3D shape reconstructions and the 3D density reconstructions, respectively. Based on these results, the quality of the reconstruction can be foreseen from a single BF-TEM image prior to the tilt-series acquisition. More precise determination of the threshold value will be achieved by conducting additional tomography experiments under imaging conditions between 1000 kV–OA1 and 400 kV–OA1 with respect to the nonlinearity. It may also be important to verify the criterion for non-crystalline materials other than amorphous carbon and for samples with multiple components.

Among some problems that must be solved to obtain quantitative tomography of micron-sized materials, the present research focused on the nonlinear intensity attenuation in BF-TEM images. However, researchers must also pay attention in actual tomography experiments to image blurring related to chromatic aberration and multiple scatterings [25,26,37,38]. The next issue should be to establish guidelines for selection of the proper OA size that balances the influences of the nonlinear attenuation, Fresnel fringes and the lateral precision.

Acknowledgements

References

1. Koguchi M, Kakibayashi H, Tsuneta R, Yamaoka M, Niino T, Tanaka N, Kase K, Iwaki M (2001) Three-dimensional STEM for observing nanostructures. *J. Electron Microsc.* 50: 235–241.

2. Midgley P A, Weyland M, Thomas J M, Johnson B F G (2001) Z-Contrast tomography: a technique in three-dimensional nanostructural analysis based on Rutherford scattering. *Chem. Commun.* 10: 907–908.

3. Yamasaki J, Tanaka N, Baba N, Kakibayashi H, Terasaki O (2004) Three-dimensional analysis of platinum supercrystals by transmission electron microscopy and high-angle annular dark-field scanning transmission electron microscopy observations. *Philos. Mag.* 84: 2819–2828.

4. Sueda S, Yoshida K, Tanaka N (2010) Quantification of metallic nanoparticle morphology on TiO_2 using HAADF-STEM tomography. *Ultramicroscopy* 110: 1120–1127.

5. Kimura K, Hata S, Matsumura S, Horiuchi T (2005) Dark-field transmission electron microscopy for a tilt series of ordering alloys: toward electron tomography. *J. Electron Microsc.* 54: 373–377.

6. Barnard J S, Sharp J, Tong J R, Midgley P A (2006) Three-dimensional analysis of dislocation networks in GaN using weak-beam dark-field electron tomography. *Philos. Mag.* 86: 4901–4922.

7. Hata S, Miyazaki H, Miyazaki S, Mitsuhara M, Tanaka M, Kaneko K, Higashida K, Ikeda K, Nakashima H, Matsumura S, Barnard J S, Sharp J H, Midgley P A (2011) High-angle triple-axis specimen holder for three-dimensional diffraction contrast imaging in transmission electron microscopy. *Ultramicroscopy* 111: 1168–1175.

8. Frank J, McEwen B F, Radermacher M, Turner J N, Rieder C L (1987) Three-dimensional tomographic reconstruction in high voltage electron microscopy. *J. Electron Microsc. Tech.* 6: 193–205.

9. Barnard D P, Turner J N, Frank J, McEwen B F (1992) A 360° single-axis tilt stage for the high-voltage electron microscope. *J. Microsc.* 167: 39–48.

10. Tanaka N, Usukura J, Kusunoki M, Saito Y, Sasaki K, Tanji T, Muto S, Arai S (2013) Development of an environmental high-voltage electron microscope for reaction science. *Microscopy* 62: 205–215.

11. Jinnai H, Tsuchiya T, Motoki S, Kaneko T, Higuchi T, Takahara A (2013) Transmission electron microtomography in soft materials. *Microscopy* 62: 243–258.

12. Koster A J, Ziese U, Verkleij A J, Janssen A H, de Jong K P (2000) Three-Dimensional transmission electron microscopy: a novel imaging and characterization technique with nanometer scale resolution for materials science. *J. Phys. Chem. B* 104: 9368–9370.

13. Klingstedt M, Miyasaka K, Kimura K, Gu D, Wan Y, Zhao D, Terasaki O (2011) Advanced electron microscopy characterization for pore structure of mesoporous materials; a study of FDU-16 and FDU-18. *J. Mater. Chem.* 21: 13664–13671.

14. Kaneko T, Nishioka H, Nishi T, Jinnai H (2005) Reduction of anisotropic image resolution in transmission electron microtomography by use of quadrangular prism-shaped section. *J. Electron Microsc.* 54: 437–444.

15. Ercius P, Weyland M, Muller D A, Gignac L M (2006) Three-dimensional imaging of nanovoids in copper interconnects using incoherent bright field tomography. *Appl. Phys. Lett.* 88: 243116.

16. Kawase N, Kato M, Nishioka H, Jinnai H (2007) Transmission electron microtomography without the 'missing wedge' for quantitative structural analysis. *Ultramicroscopy* 107: 8–15.

17. Kato M, Kawase N, Kaneko T, Toh S, Matsumura S, Jinnai H (2008) Maximum diameter of the rod-shaped specimen for transmission electron microtomography without the 'missing wedge'. *Ultramicroscopy* 108: 221–229.

18. Saghi Z, Xu X, Möbus G (2008) Electron tomography of regularly shaped nanostructures under non-linear image acquisition. *J. Microsc.* 232: 186–195.

19. Van den Broek W, Rosenauer A, Goris B, Martinez G T, Bals S, Van Aert S, Van Dyck D (2012) Correction of non-linear thickness effects in HAADF STEM electron tomography. *Ultramicroscopy* 116: 8–12.

20. Zhang H B, Zhang X L, Wang Y, Takaoka A (2007) Tomography experiment of an integrated circuit specimen using 3 MeV electrons in the transmission electron microscope. *Rev. Sci. Instrum.* 78: 013701.

21. Zhang H, Takaoka A, Miyauchi K (1998) A 360°-tilt specimen holder for electron tomography in an ultrahigh-voltage electron microscope. *Rev. Sci. Instrum.* 69: 4008–4009.

22. Kamino T, Yaguchi T, Konno M, Ohnishi T, Ishitani T (2004) A method for multidirectional TEM observation of a specific site at atomic resolution. *J. Electron Microsc.* 53: 583–588.

23. Reimer L, Kohl H (2008) *Transmission electron microscopy*, 5th ed., Chap. 6 (Springer, New York).

24. Zhang H B, Wang F, Takaoka A (2007) Measurement of electron transmission through tilted thick specimens with an ultrahigh voltage electron microscope. *J. Electron Microsc.* 56: 51–55.

25. Wang F, Zhang H B, Cao M, Nishi R, Takaoka A (2010) Multiple scattering effects of MeV electrons in very thick amorphous specimens. *Ultramicroscopy* 110: 259–268.

26. Oshima Y, Nishi R, Asayama K, Arakawa K, Yoshida K, Sakata T, Taguchi E, Yasuda H (2013) Lorentzian-like image blur of gold nanoparticles on thick amorphous silicon films in ultra-high-voltage transmission electron microscopy. *Microscopy* 62: 521–531.

27. Brooks R A, Di Chiro G (1976) Beam hardening in X-ray reconstructive tomography. *Phys. Med. Biol.* 21: 390–398.

28. Hammersberg P, Mangard M (1998) Correction for beam hardening artefacts in computerised tomography. *J. X-Ray Sci. Technol.* 8: 75–93.

29. Krumm M, Kasperl S, Franz M (2008) Reducing non-linear artifacts of multi-material objects in industrial 3D computed tomography. *NDT&E Int.* 41: 242–251.

30. Motojima S, Kawaguchi M, Nozaki K, Iwanaga H (1990) Growth of regularly coiled carbon filaments by Ni catalyzed pyrolysis of acetylene, and their morphology and extension characteristics. *Appl. Phys. Lett.* 56: 321–323.

31. Kawaguchi M, Nozaki K, Motojima S, Iwanaga H (1992) A growth mechanism of regularly coiled carbon fibers through acetylene pyrolysis. *J. Cryst. Growth* 118: 309–313.

32. Du J-H, Sun C, Bai S, Su G, Ying Z, Cheng H-M (2002) Microwave electromagnetic characteristics of a microcoiled carbon fibers/paraffin wax composite in Ku band. *J. Mater. Res.* 17: 1232–1236.

33. Yamamoto K, Hirayama T, Kusunoki M, Yang S, Motojima S (2006) Electron holographic observation of micro-magnetic fields current-generated from single carbon coil. *Ultramicroscopy* 106: 314–319.

34. Yoshimura K, Nakano K, Miyake T, Hishikawa Y, Kuzuya C, Katsuno T, Motojima S (2007) Effect of compressive and tensile strains on the electrical resistivity of carbon microcoil/silicone-rubber composites. *Carbon* 45: 1997–2003.

35. Hashimoto A, Shimojo M, Mitsuishi K, Takeguchi M (2009) Three-dimensional imaging of carbon nanostructures by scanning confocal electron microscopy. *J. Appl. Phys.* 106: 086101.

36. Williams D B, Carter C B (1996) *Transmission electron microscopy*, Chap. 6 (Plenum Press, New York).

37. Motoki S, Kaneko T, Aoyama Y, Nishioka H, Okura Y, Kondo Y, Jinnai H (2010) Dependence of beam broadening on detection angle in scanning transmission electron microtomography. *J. Electron Microsc.* 59: S45–S53.

38. Wang F, Zhang H-B, Cao M, Nishi R, Takaoka A (2011) Image blurring of thick specimens due to MeV transmission electron scattering: a Monte Carlo study. *J. Electron Microsc.* 60: 315–320.